APPLICATION OF REACTIVE DISCRETE EQUATION METHOD TO THE ENACCEF TEST 13H

Kudriakov S.[1], Beccantini A.[2]
[1]CEA/LTMF, 91191, Gif-sur-Yvette, France, skudriakov@cea.fr,
[2]CEA/LTMF, 91191, Gif-sur-Yvette, France, alberto.beccantini@cea.fr,

ABSTRACT

The Reactive Discrete Equation Method (RDEM) was recently introduced in [1, 2], adapted to combustion modelling in [3] and implemented in the TONUS code [4]. The method has two major features: the combustion constant having velocity dimension *is the fundamental flame speed*, and the combustion wave now is an integrable part of the Reactive Riemann Problem. In the present report the RDEM method is applied to the simulation of the combustion Test 13H performed in the ENACCEF facility. Two types of computations have been considered: one with a constant fundamental flame speed, the other - with time dependent fundamental flame speed. It is shown that by using the latter technique we can reproduce the experimental visible flame velocity. The ratio between the fundamental flame speed and the laminar flame speed takes, however, very large values compared to the experimental data based on the tests performed in spherical bombs or cruciform burner.

1 Introduction

During anticipated accidents in buildings containing hydrogen fueled equipment, hydrogen gas can be continuously or instantaneously released into the surroundings. This can happen, for example, in a public or private garage through faulty valves or seals of a hydrogen tank, or following a vehicle accident in a tunnel. Depending on the local concentration and/or presence and activation of mitigation devices, hydrogen may burn following different combustion regimes. These regimes may include jet fires, slow deflagrations, fast deflagrations and detonations depending on the combustion process development. Thus, one has to estimate the severity of a combustion process under given geometrical configuration, scale and composition of combustible mixture. Here the issue is not to predict details of turbulent flame structure and propagation, but rather to evaluate the possible flame speeds and the corresponding dynamic pressure loadings which might be generated during combustion. These data then can be used in structural analysis codes to verify the integrity of the structure.
A number of studies on hydrogen combustion in industrial-type geometries has been performed previously using the CREBCOM (CRiteria and Experimentally Based COmbustion Model) [5]. This model, developed at the Kurchatov Institute, is devoted to study of combustion in geometries which are much larger than the characteristic dimensions of the physical phenomena involved. Thermal conduction and species diffusion, which are responsible for the propagation of deflagrations, are not directly modelled; their action is taken into account by introducing an experimentally derived correlation source term into the Euler equations. The model has been successfully implemented in several industrial purpose CFD codes, including TONUS code [4] and COM3D code [6] to investigate turbulent combustion flows. It suffers, however, from two main drawbacks:

- a burning rate constant, present in the source term of Euler equations, has the dimensions of a speed. This speed is correlated to the fundamental flame speed, and the correlations are grid-, and problem-dependent [7].
- the algorithm involves a binary criterion function that specifies when a control volume is to be burnt. Numerical experiments have shown that, as the flame speed is low with

respect to the speed of sound, the criterion function can create numerical oscillations in the pressure that strongly affect the flow [8].

In the literature there exist several other approaches that model flames as interfaces. Some of them, like the RDEM approach, require the solution of the reactive Riemann problem between the burnt and unburnt regions. The solution of the Riemann problem for the reactive Euler equations is the object of [9] in the particular case of calorically perfect gases, under the hypothesis of weak deflagration, Chapman-Jouguet deflagration, Chapman-Jouguet detonation or strong detonation regimes. Unfortunately, the eventual existence of a rarefaction wave (Taylor wave) behind the Chapman-Jouguet deflagration is not taken into account in the work, which makes impossible the modelling of the deflagration-to-detonation transition in a continuous way. In [3], the existence of the Taylor wave behind a Chapman-Jouguet deflagration is taken into account; moreover the variation of the specific heats with temperature is considered.
In the present paper the RDEM method is applied to the simulation of the combustion Test 13H performed in the ENACCEF facility. The paper is organized as follows. After this introduction, in Section 2 we give a general description of the ENACCEF facility as well as the analysis of the Test 13H experimental data. In Section 3 we briefly present the governing equations and the underlying hypothesis; the way the equations are discretized is discussed in Section 4. Presentation and analysis of the computed results is given in Section 5. The final conclusions make the subject of Section 6.

2 ENACCEF Test 13H: General Description and Analysis

2.1 Test Facility: Description and Geometrical Data [10]

ENACCEF (ENceinte d'ACCElération de Flamme) is located at the Laboratoire Combustion et Système Réactive (LCRS) of Institut de Combustion Aérothermique Réactivité et Environnement (ICARE) of Orleans. View of ENACCEF facility together with the sketch of different parts are presented on Fig. 1. The facility is 5 m of height and is made of Z3CN18-10 stainless steel. It is divided into two parts:

- the acceleration tube (3.2 m long and 154 mm i.d.), in which repeated obstacles of various geometries can be inserted;
- the dome (1.7 m long, 738 mm i.d.).

The acceleration tube is equipped with two tungsten electrodes at 0.138 m from the bottom of the facility as a low-energy ignition device. The energy delivered is estimated to be around 10-20 mJ. Different obstacles of varying blockage ratio can be installed inside the tube. For the test, which we shall describe in the next subsection, nine annular obstacles of blockage ratio 0.63 have been installed in the acceleration tube; the first one being 0.638 m from the ignition point, and the distance between obstacles was fixed to 0.154 m.
ENACCEF facility is highly instrumented to follow the flame propagation: 16 UV-sensitive photomultiplier tubes (HAMAMATSU, 1P28) are mounted across silica windows (optical diameter: 8 mm, thickness: 3 mm) in order to detect the flame as it propagates (5 photomultiplier tubes are located along the dome and 11 - along the acceleration tube).
Several high speed pressure transducers, (7 from CHIMIE METAL, 1 PCB and 1 KISTLER) are mounted flush with the inner surface of the tube in order to monitor the pressure variation in the tube as the flame propagates, and the pressure buildup is monitored via a Kistler pressure transducer mounted at the ceiling of the dome. Gas sampling is used to measure the gas composition along the facility. Five gas samplings are located along the acceleration tube and one - in the dome.

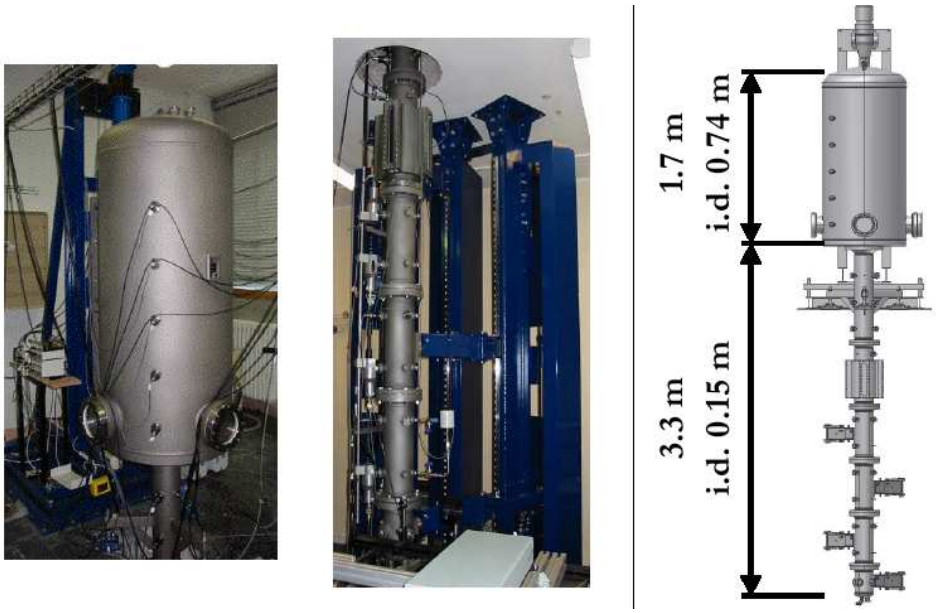

Figure 1: View of ENACCEF facility (left) and sketch of its different parts (right). Scanned from [10].

2.2 Test 13H: Initial Conditions

The ENACCEF Test 13H on hydrogen combustion has been dedicated to a homogeneous gas distribution in a containment volume. The initial gas mixture composition and thermodynamic conditions are: $P_{init.} = 10^5$ Pa, $T_{gas-init.} = 298$ K; $X_{H_2} = 0.13$, and $X_{Air} = 0.87$. The gases are provided by Air Liquid. The purity of hydrogen is 99.999 %. The air used in the experiment is the mixture of nitrogen and oxygen with the proportion: (80% N_2 + 20% O_2) [10].

2.3 Test 13H: Flame Velocity and Pressure Measurements.

Experimental flame velocity is computed using the flame arrival times at the consecutive photomultipliers and the distance between them. Using the simple linear formula the flame velocities were computed for 24 runs, and are represented at the points which are mean positions between consecutive photomultipliers locations on the Fig. 2 (left). The error bars show flame velocity spread at each location. The measured flame velocities in the dome area are not shown here due to rather large spread. In fact, if the flame front is highly disturbed and presents a 3D structure with rolls, the flame position will be less precise as the detectors collect light along a solid angle and not at a line of sight. This, together with a larger solid angle, presents a problem of flame velocity measurements in the dome.
Three phases of flame propagation inside the acceleration tube can be clearly distinguished:

- low flame velocity, equal to about 15-20 m/s at the initial, non-obstructed part of the acceleration tube;
- strong flame acceleration up to 500-600 m/s in the obstructed area;
- flame deceleration down to 300-400 m/s in the upper non-obstructed part.

On the Fig. 2 (right) we present the pressure evolution with time measured with Kistler transducer located at the top of the dome. The pressure evolution measured by Kistler transducer is close to the Adiabatic Isochoric Complete Combustion (AICC) value for overpressure of 4.0772 bar.

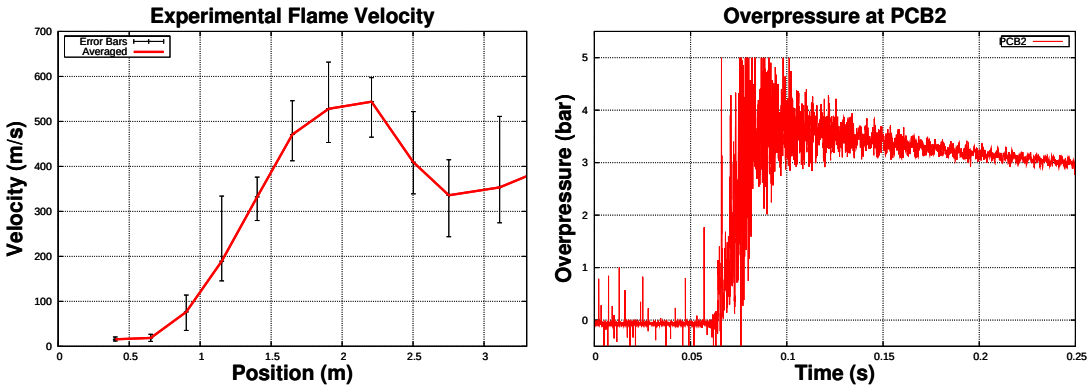

Figure 2: Averaged experimental flame velocities in the acceleration tube. Vertical error bars represent standard deviation of the velocity data point based on multiple tests (left), and experimental over-pressure at the top of the dome (right).

The pressure is close to the initial value during initial 60 ms and then starts to rise upto AICC values. It should be noted that the volume ratio between the acceleration tube and the dome is 1 : 12.2. During the flame propagation along the acceleration tube only small fraction of hydrogen is burnt and some part of it is vented into the dome. Due to large volume ratios this does not lead to a noticeable pressure increase in the dome. It is when the flame develops inside the dome, we observe the rapid pressure rise. This is confirmed by looking at the flame time of arrival in the dome, more precisely, at the location 14 cm higher than the upper rim of the acceleration tube. The time of arrival oscillates around 40 ms which is about 20 ms before the beginning of pressure rise.

3 Physical modelling

In this section we present the governing equations we are going to solve together with the underlying hypotheses. The more detailed explanation and hypotheses justification can be found in [3].
We restrict our attention to ideal gas mixtures. The chemical evolution is assumed to be governed by one irreversible, infinitely fast chemical reaction between hydrogen and oxygen $H_2 + \frac{1}{2}O_2 \rightarrow H_2O$. We do not take into account the thermal diffusivity and the species diffusion.
The molar and mass fraction variations during the chemical reaction are linked via

$$\frac{\Delta X_{H_2}}{1} = \frac{\Delta X_{O_2}}{1/2} = \frac{\Delta X_{H_2O}}{-1}, \quad \frac{\Delta Y_{H_2}}{W_{H_2}} = \frac{\Delta Y_{O_2}}{0.5\, W_{O_2}} = -\frac{\Delta Y_{H_2O}}{W_{H_2O}} \tag{1}$$

where W_j is the molar weight of the j-th species.

3.1 Governing equations

We consider here initially homogeneous mixtures of perfect gases. The system of equations we want to solve is given by

$$\begin{cases} \dfrac{\partial}{\partial t}\rho + \vec{\nabla}\cdot(\rho\vec{w}) = 0 \\ \dfrac{\partial}{\partial t}(\rho\vec{w}) + \vec{\nabla}\cdot(\rho\vec{w}\otimes\vec{w} + P) = 0 \\ \dfrac{\partial}{\partial t}(\rho\tilde{e}_t) + \vec{\nabla}\cdot(\rho\vec{w}\tilde{h}_t) = 0 \\ \dfrac{\partial}{\partial t}(\xi) + \vec{D}\cdot\vec{\nabla}\xi = 0 \end{cases} \tag{2}$$

ρ being the total density (kg/m^3 in the SI units), $\vec{w}$ the velocity (m/s), P the pressure (Pa), $\tilde{e}_t$ ($\tilde{h}_t$) the specific total (sensible plus formation plus kinetic) energy (enthalpy) (J/kg), $\vec{D}$ the visible flame speed.
P is linked to the internal energy via the equation of state (EOS). In our case

$$P = \rho\left(\sum_j Y_j\frac{\mathcal{R}}{W_j}\right)T,\ \tilde{e}_t = \tilde{e} + \frac{1}{2}w^2,\ \tilde{h}_t = \tilde{e}_t + \frac{P}{\rho}$$
$$\tilde{e} = \sum_j Y_j h_j^0 + e = \sum_j Y_j h_j^0 + \int_0^T \left\{\sum_j Y_j c_{v,j}(\alpha)\right\}\mathrm{d}\alpha$$

where $\mathcal{R}$ is the universal gas constant ($\mathcal{R} = 8.314$ J/mol/K), T the mixture temperature (K in SI units), W_j (kg/mol) $c_{v,j}(T)$ (J/kg/K) and h_j^0 (J/kg) the molar weight, the constant volume specific heat and the formation enthalpy at 0 K of the species j, e the (sensible) internal energy (J/kg). The progress variable $\xi(\vec{r},t)$ for the chemical reaction is related to the hydrogen mass fractions $Y_{\mathrm{H_2,i}}(\vec{r},t)$ and $Y_{\mathrm{H_2,f}}(\vec{r},t)$ before and after the combustion by

$$\xi(\vec{r},t) = \frac{Y_{\mathrm{H_2}}(\vec{r},t) - Y_{\mathrm{H_2,i}}(\vec{r},t)}{Y_{\mathrm{H_2,f}}(\vec{r},t) - Y_{\mathrm{H_2,i}}(\vec{r},t)}, \tag{3}$$

Since the chemical reaction is assumed to be infinitely fast, the progress variable will be either 1 (in the burnt region) or 0 (in the unburnt region).
The first three equations represent the conservation equations for mass, momentum and energy. Using the values for ξ, we can recover the instantaneous mass fractions (used in the EOS). Indeed for hydrogen it is

$$Y_{\mathrm{H_2}} = Y_{\mathrm{H_2,i}} + \xi(Y_{\mathrm{H_2,f}} - Y_{\mathrm{H_2,i}}).$$

In case of complete combustion,

$$Y_{\mathrm{H_2,f}} = \max\left(0, Y_{\mathrm{H_2,i}} - \frac{W_{\mathrm{H_2}}}{0.5W_{\mathrm{O_2}}}Y_{\mathrm{O_2,i}}\right).$$

For the j-th species

$$Y_{\mathrm{j}} = Y_{\mathrm{j,i}} + \xi(Y_{\mathrm{j,f}} - Y_{\mathrm{j,i}})$$

where $(Y_{\mathrm{j,f}} - Y_{\mathrm{j,i}})$ is linked to $(Y_{\mathrm{H_2,f}} - Y_{\mathrm{H_2,i}})$ via equation (1).
The fourth equation in (2) is the transport equation for the progress variable ξ. This equation is in non-conservative form. As one can read in [1], since ξ is 0 in the unburnt region and

1 in the burnt one, far from the reactive interface this equation is satisfied (the LHS of the equation is zero); then $\vec{D}$ needs to be defined only on the interface (with the same value ahead and behind it) and represents its velocity. $\vec{D}$ is computed here as function of the fundamental flame speed K_0 via

$$\vec{D} = \vec{w} + K_0 \vec{n}_\alpha, \tag{4}$$

where $\vec{n}_\alpha$ is the normal to the flame surface going from the burnt to the unburnt region, $\vec{w}$ the velocity of the unburnt gas.
Concluding, our final purpose is the solution of the system of equations (2). The dependent variables are ρ, $\rho\vec{w}$, $\rho\tilde{e}_t$, and ξ. At the beginning we know the initial conditions for these variables. The fundamental flame speed K_0 can be a function of space and time; in this work we consider it to be either a constant or a function of time only.

4 Numerical Modelling

The system of equations (2) is solved using Finite Volume approach. We use the approximate Riemann solution to the reactive Riemann problem described in [3]. The solution of the reactive Riemann problem requires the flame surface location which is determined using the Discrete Equation Method described below.

4.1 RDEM for the reactive Euler equations

The full description of the Reactive Discrete Equation Method (RDEM) can be found in [2]. In this subsection we give a brief summary of its main features.

- The DEM and RDEM are *Eulerian approaches*, although their extension to the Arbitrary Lagrangian Eulerian (ALE) approach is straightforward.
- The methods are used for studying multiphase mixtures, in which global averaging of a variable in a control cell could lead to unacceptable numerical errors. In these approaches *each phase has its own set of variables.*
- DEM has been introduced in [1].
- DEM has been modified into RDEM and used, *coupled with a reactive Riemann solver,* to study *evaporation front propagations* and *detonation propagations* [2].
- RDEM is used in [3] to study flame front propagation in a deflagration and a detonation regimes.
- Both approaches are conservative, i.e. the extensible quantity taken from one phase is given to the other.

The description of the RDEM approach is the object of [2] in the case of evaporation front progagation; the adaption of this approach to combustion problem has been possible thanks to solution of the Reactive Riemann problem at all combustion regimes [3]. Indeed, as suggested in [11], the reaction wave, in the same manner as an evaporation wave, can be considered as a phase boundary which separates the "unburnt gas" phase (phase 1) from the "burnt gas" phase (phase 2); thus, across the reactive shock we have a "phase transition" between the "unburnt mixture" phase and the "burnt mixture" phase.
We emphasize that, in several spatial dimensions, the reactive Riemann problem is solved in each spatial direction. As explained in [3], the flame speed is given by $\vec{D} = \vec{w} + K_0\vec{n}_\alpha$, $\vec{n}_\alpha$ being the normal to the flame surface going from the burnt to the unburnt mixture (i.e. $\vec{n}_\alpha \propto \vec{\nabla}\alpha$, α being the fraction volume of one phase). Then when we want to compute the numerical flux in the $(\vec{n}, \vec{t})$ frame of an interface of a cell volume (Finite Volume approach), we have to solve a 1D Riemann problem with a fundamental flame speed equal to $K_0(\vec{n}\cdot\vec{n}_\alpha)$.

5 Numerical Results

In the present report we explore two cases: K_0 is constant in space and time, and K_0 is a time variable.
The first case, i.e. the case of constant K_0, is used in order to test the grid convergence of the numerical solution. We test it in terms of computed visible flame velocity in the tube, as well as flame surface evolution. By using the time variation of the fundamental flame speed, i.e. $K_0 = K_0(t)$, we try to reproduce the experimental values for a visible flame velocity. This will allow us to analyze the values of the fundamental flame speed in terms of the corresponding values of the visible flame speed.

5.1 Constant value of fundamental flame speed

There are two main factors responsible for flame acceleration: increase of the flame surface due to interactions of gas flow with obstructions and increase of the burning rate with the turbulence level. In this section only the first one was accounted for.
We applied the following strategy: first, compute the flame speed on the coarse grid (RAF 1), using the value of K_0 such that the computed visible flame velocity is close to the experimental one, and second, make the computation with the same K_0 on the refined grids (RAF2, RAF3, and RAF4). The idea behind is to study the grid convergence in terms of flame velocity and flame surface.
The computations have been done assuming the axial symmetry of the solution, and the numerical grids are presented on the Fig. 3. For the coarse grid the tube radius is divided into 7 elements. This number is doubled for the second level of refinement, tripled - for the third, and quadrupled - for the fourth. The segments along the axis of symmetry are refined accordingly. The obstacles in the tube are represented by the cracks in the mesh (see Fig. 3, zoomed part), so that the neighboring elements are slightly skewed. In the dome the elements are not uniform: their linear sizes gradually increase up to three times along the radius, and up to four times - along the axis of symmetry.

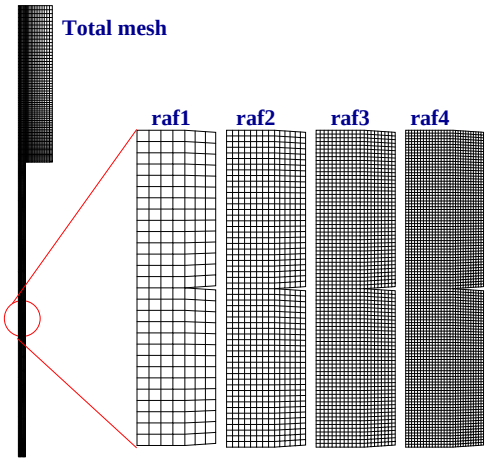

Figure 3: Numerical grids used for the computation. The coarse grid (RAF1) is composed of 3585 elements, grid RAF2 - of 14283 elements, grid RAF3 - of 32201 elements, and grid RAF4 - of 57160 elements.

The results for the flame speed corresponding to the coarse mesh (RAF1, green curve on the Fig. 4 (left)) are obtained by trial and error in such way as to have the computed values for flame velocity within the error bars of the experimental flame velocity at as many points as possible. The value of the fundamental flame velocity in this case is $K_0 = 10$ m/s. It appears that by using a single values for the fundamental flame speed K_0 we can not reproduce the

experimental curve: K_0 has to be relatively low in the initial non-obstructed part of the tube, and sufficiently high at the obstructed area.
By looking at the computed visible flame velocity obtained on different grids for $K_0 = 10$ m/s (Fig. 4 (left)) we observe *1)* a remarkable difference between the results corresponding to the coarse grid and the results corresponding to the finer grids, and *2)* a relatively small difference between the results corresponding to grids RAF2, RAF3, and RAF4 in the initial non-obstructed part, and in the most of obstructed part.
Lower numerical viscosity relate to the finer grids leads to a higher gas velocity along the center-line at the flame location, which in turn leads to a higher flame stretch. Flame surface evolutions are close to each other when the flame crosses first six obstacles, while further downstream the curves diverge: the evolution corresponding to the finest mesh (RAF4) is generally higher than the others. This can be explained by the higher amplitudes of the gas velocity; at the last obstacle the gas velocity corresponding to the finest mesh is 100 m/s higher than the velocities corresponding to other grids.

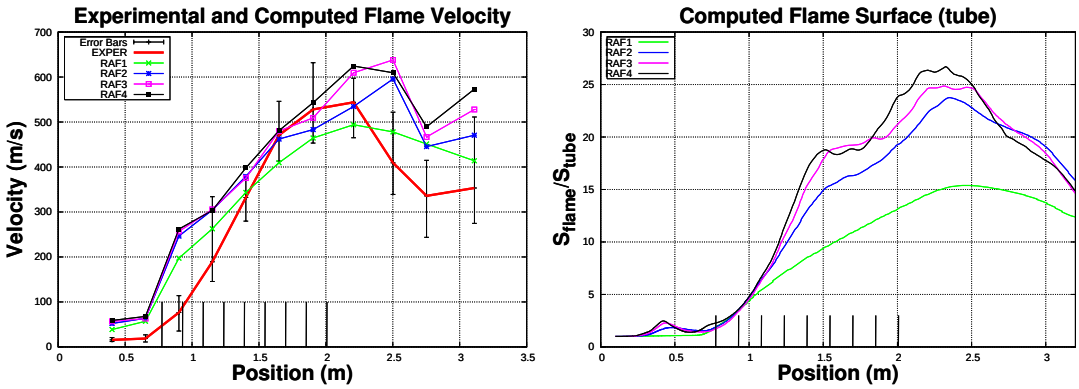

Figure 4: Flame velocity computed for different grids and compared with the experimental flame velocity (left), and non-dimensionalized flame surface computed for different grids (right). Obstacle positions are shown by short vertical lines. $K_0 = 10$ m/s.

From the Figure 4 (right) we can see that a flame surface increases while flame crosses the obstacle-laden part. It reaches its maximum value at a position which is 3 to 4 diameters downstream the last obstacle, and this value varies between 15 and 27 tube cross sections, depending on the mesh. This rather big value for the flame surface can be explained by the presence of certain number of unburnt gas pockets between the obstacles, seen on Fig. 5 (right). The progress variable distribution is shown there at the time when the flame surface has its maximum value. Soon after the time of reaching the maximum value for flame surface area, the fresh gas in the pockets is consumed, which inevitably leads to diminishing of the flame surface area. The progress variable distributions show highly diffused flame computed using the coarse grid (RAF1). In the case of the other grids flame distributions show similar trends: it spreads between seven obstacles.
The flame surface spread between several obstacles in obstructed channels has been observed experimentally as well. There exist, however two major differences between the experimental results and the present numerical results conditioned by the modelling capabilities. In fact in the combustion model there is no mechanism of flame quench/extinction. Experimentally the flame might cease to exist between certain obstacles, which would lead to smaller values of flame surface. Another difference lies in the fact that K_0 is a *constant everywhere in the domain*. Recent experimental results [12] show that a flame (stoichiometric methane-air mixture used in the reference) in a obstructed channel with BR=0.67 exhibits different behavior depending on the flame position. The flame surface consists of a laminar flame tip propagating downstream in the channel core and the rest of the flame surface in the turbulent regime propagates transversely into the recirculation zones between obstacles. As

a future work we suggest to perform the computation using variable in space values of K_0 in order to capture the experimental flame behavior.
The maximum value of the flame surface is reached when the flame exits the obstacle area and propagates further 3 to 4 diameters downstream. At that time there still exist pockets of unburnt gas (see Fig. 5) as well as the mushroom-like shape of the flame in the obstacle-free part, visible in the pictures corresponding to finer grids.

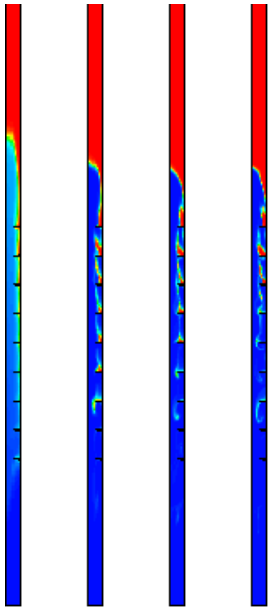

Figure 5: Progress variable distribution at the time when the flame surface reaches its maximum value in the tube. Results correspond to grids *RAF1* at $t = 19.75$ ms, *RAF2* at $t = 16.78$ ms, *RAF3* at $t = 16.03$ ms, and *RAF4* at $t = 15.45$ ms (from left to right). $K_0 = 10$ m/s. Red color corresponds to unburnt mixture, blue color - to burnt mixture.

5.2 Variable value of fundamental flame speed.

As it was mentioned in the previous subsection, the constant value of K_0 does not allow us to reproduce the averaged experimental visible flame velocity evolution: we have either too high velocity in the initial obstacle-free part of the tube, or too low velocity at the upper part of the obstructed area. In this subsection we shall change the value of the fundamental flame speed with time in order to have a visible flame speed as close as possible to the experimental one. This will allow us to analyze the *fundamental flame speed* evolution.
From the previous subsection we can see that the results computed using the coarse mesh RAF1 suffer from an excessive diffusion, while the results corresponding to the other grids show similar behavior at least in the most part of the tube. Due to the fact the trial-and-error computation requires considerable number of tests, we prefer to use the grid RAF2 in order to have a reasonable CPU time.
On the Fig. 6 (left) we present the comparison between the experimental visible flame velocity and the computed visible flame velocity. The computed curve is entirely within the error bars of the experimental curve. This was possible due to dynamic change of value of K_0 during the computation. These values together with their application intervals are indicated on the Fig. 6 (left). First of all we would like to mention that the ratio between the numerical values for K_0 and the laminar flame velocity (taken at initial thermodynamic conditions) varies from 14.55 to 112 during the flame acceleration in the tube. These values for ratio are high compared with the experimental values for the ratio between turbulent fundamental flame speed and laminar flame speed which do not exceed 20 (see [13] and

references therein).
Another point deserving attention is the excessively low value for K_0 in the region after 2.3 meters, i.e two diameters downstream of obstructed part. We had to impose excessively low value ($K_0 = 0.01$ m/s) in order to recover the negative gradient of the experimental flame velocity. We note in passing that experiments performed in ENACCEF using a hydrogen-air mixture with negative hydrogen concentration gradient going from 11.4 % at the tube bottom down to 6.7 % at the top of the tube show that *flame is always quenched in the upper part of the tube.* This indicates that the important flame stretch together with enhanced mixing lead in this situation to low values of the fundamental flame velocity. In our case the mixture is more reactive (13 % of hydrogen), therefore the flame "survives" and continues to propagate.

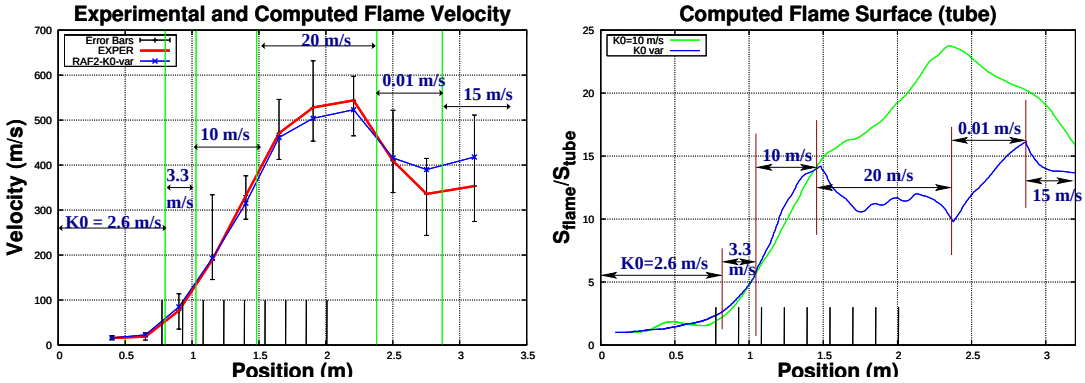

Figure 6: Flame velocity computed using grid RAF2 (blue curve) is compared with the experimental flame velocity (red curve) (left). adimensionalized flame surface computed using constant value of K_0 (green line), and variable values of K_0 (blue line) (right) Obstacle positions are shown by short vertical lines. Values of K_0 are indicated together with the application intervals.

The flame surface evolution computed using the variable in time values of K_0 shows similar behavior to the evolution corresponding to the constant K_0 value upto the distance $Z = 1.5$ m. When the fundamental flame velocity is increased twofold, from 10 m/s to 20 m/s, the flame surface decreases and oscillates around $12 \times S_{tube}$. This decrease we attribute to the rapid burn-out of the fresh gas pocketed between the obstacles. This is confirmed by looking at the progress variable distribution at time $t = 50.35$ ms, i.e. time when the flame surface reaches the value $10 \times S_{tube}$. There is almost no unburnt gas downstream of the flame.

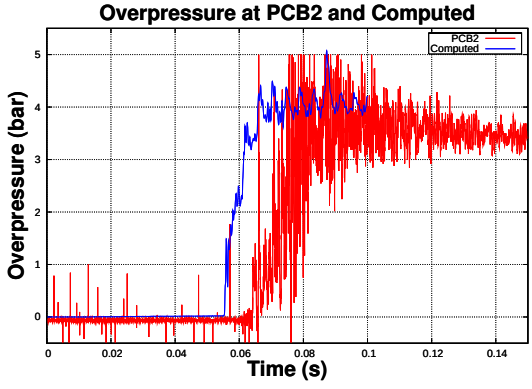

Figure 7: Computed pressure evolution in the upper part of the dome (blue line) compared with the experimental pressure evolution (red line).

The computed overpressure evolution at the transducer located in the upper part of the dome is compared with the corresponding experimental overpressure evolution on the Fig. 7. We have shown in the Section 3 that the pressure rise corresponds to the flame propagation

inside the dome. It means that in order to correctly model the pressure rise gradient one has to correctly model flame velocity and flame surface development inside the dome. This is outside the scope of the present report as there are very limited experimental data. The computed asymptotic values for the overpressure oscillates around a value close to 4.1 bar which is near the AICC value of 4.077 bar.

6 Conclusions

In this paper the RDEM method is applied to the simulation of the combustion Test 13H performed in the ENACCEF facility. Two cases were explored:

- K_0 is constant in space and time, i.e. increase of the flame surface due to only interactions of gas flow with obstructions is accounted;
- K_0 is a time variable, i.e. in addition to the above phenomenon, a change of the burning rate with time uniformly in space is considered.

The first case, i.e. the case of constant K_0, is used in order to test the grid convergence of the numerical solution. We test it in terms of computed visible flame velocity in the tube, as well as flame surface evolution. We show that grid convergence is achieved in terms of the above mentioned variables, and the solutions corresponding to three of the four meshes considered are similar. This allowed us to use a second grid, called RAF2, for making a numerical experiment with time varying K_0. The goal is to reproduce experimental visible flame speed. The values of fundamental flame velocity K_0 were compared to laminar flame speed, which showed that their ratio is up to six times greater than the corresponding experimental ratio.
As a future work, we suggest to perform a computation with a variable in space and time value of K_0 by taking into account pressure, temperature, and shear stress effects.

Acknowledgments
We emphasize that the implementation of the RDEM approach in the TONUS code has been partially financed by the Institut de Radioprotection et de Sûreté Nucléaire (IRSN). The authors are grateful to Dr. A. Bentaib and Dr. N. Chaumeix for providing experimental data and for fruitful discussions.

References

[1] Abgrall R., Saurel R. Discrete equations for physical and numerical compressible multiphase mixtures. *Journal of Computational Physics* 2003; **186**: 361-396.

[2] Le Métayer O., Massoni J., Saurel R. Modelling evaporation fronts with reactive Riemann solvers. *Journal of Computational Physics* 2005; **205**: 567-610.

[3] Beccantini A. and Studer E. The reactive Riemann problem for thermally perfect gases at all combustion regimes. *International Journal for Numerical Methods in Fluids.* 2009.

[4] Kudriakov S., Dabbene F., Studer E., Beccantini A., Magnaud J.P., Paillère H., Bentaib A., Bleyer A., Malet J., Porcheron E., Caroli C. The TONUS CFD code for hydrogen risk analysis: Physical models, numerical schemes and validation matrix. *Nuclear Engineering and Design* 2008: **238**: 551-565.

[5] Efimenko A.A., Dorofeev S.B., CREBCOM code system for description of gaseous combustion, *Journal of Loss Prevention in the Process Industries*, 2001; **14**, 575-581.

[6] Bielert U., Breitung W,. Kotchourko A., Royl P., Scholtyssek W., Veser A., Beccantini A., Dabbene F., Paillere H., Studer E., Huld T., Wilkening H., Edlinger B., Poruba C., Mohaved M. Multi-dimensional simulation of hydrogen distribution and turbulent combustion in severe accidents. *Nuclear Engineering and Design* 2001; **209**: 165-172.

[7] Dorofeev S., Redlinger R., Description of FLAME3D, Internal report. Forschungszentrum, IKET, Karlsruhe, 2003.

[8] Gallego E., Garcia J., Migoya E., Crespo A., Kotchourko A., Yanez J., Beccantini A., Hansen O.R., Baraldi D., Hoiset S., Voort M.M., Molkov V. An inter-comparison exercise on the capabilities of CFD models to predict deflagration of a large-scale H2-air mixture in open atmosphere. *International Conference on Hydrogen Safety*. Pisa, September 8-10 2005.

[9] Teng Z.H., Chorin A.J., Liu T.P., Riemann problems for reacting gas, with applications to transition. *SIAM Journal of Applied Mathematics* 1982; **42**:964-981.

[10] Malet F. Etude expérimentale et numérique de la propagation de flammed prémélangées turbulentes dans une atmosphère pauvre en hydrogène et humide. PhD Thesis, Université d'Orléans, 2005.

[11] Colombo RM, Corli A. Sonic hyperbolic phase transitions and Chapman-Jouguet detonations. *Journal of Differential Equations* 2002; **184**: 321-347.

[12] Johansen C.T., Ciccarelli G., Visualisation of the unburned gas flow ahead of an accelerating flame in an obstructed square channel, *Combustion and Flame*, 2009; **156**, 405-416.

[13] Shy S.S., Lin W.J., Peng K.Z., High-Intensity Turbulent Premxed Combustion: General Correlations of Turbulent Burning Velocities in a New Cruciform Burner, *Proceedings of the Combustion institute* 2000; **28**: 561-568.